RSC Advances

PAPER

View Article Online
View Journal | View Issue

Cite this: *RSC Adv.*, 2022, **12**, 18238

A theoretical study on the on–off phosphorescence of novel Pt(II)/Pt(IV)–bisphenylpyridinylmethane complexes†

Guoxun Zhu,[a] Zhenping Chen,[a] Huacan Song,[ab] Ao You*[c] and Zhengquan Li*[a]

An in-depth theoretical study on the Pt(II)/Pt(IV)–bisphenylpyridinylmethane complexes was carried out, which focused on the geometric/electronic structures, excitation procedures, on–off phosphorescence mechanisms, and structure–optical performance relationships. The key roles of the linkages (LK) connected in the middle of phenylpyridines were carefully investigated using multiple wavefunction analysis methods, such as non-covalent interaction (NCI) visualizations and natural bond orbital (NBO) studies. The phosphorescence-off phenomenon was considered by hole–electron analysis and visualizations, spin–orbit coupling (SOC) studies, and NBO analysis. Through these investigations, the relationship of the substituents in LK and the optical performances were revealed, as well as the fundamental principles of the phosphorescence-quenching mechanism in Pt(IV) complexes, which pave the way for further performance/structural renovation works. In addition, an intuitive visualization method was developed using a heatmap to quantitatively express the SOC matrix elementary (SOCME), which is helpful for big data simplification for phosphorescence analysis.

Received 15th May 2022
Accepted 7th June 2022

DOI: 10.1039/d2ra03060h

rsc.li/rsc-advances

Introduction

Taking advantage of the special reactivities of Pt and adjustable properties of ligands, Pt complexes have been widely applied in catalysis,[1a] medical fields,[1b,c] trace detection of ions/organic compounds,[1d,e] identification of biostructures,[1f] and optical applications.[1g] The biocompatibility and photosensitivity of Pt have inspired Pt-based photoactivatable prodrugs design, and a lot of novel Pt complexes have been synthesized to explore the structure–activity relationships.

For instance, Sadler's group synthesized *trans*,*trans*,*trans*-[Pt(py)$_2$(N$_3$)$_2$(biotin)(OH)] and *trans*,*trans*,*trans*-[Pt(py)$_2$(N$_3$)$_2$(-biotin)(DCA)] by an esterification reaction[2a] (Fig. 1a), through which the binding properties to avidin and the aqueous solubility were improved. The products exhibited high visible light photocytotoxicities, which showed potential in phototherapy. Shao and co-workers prepared two Pt complexes ([Pt(bpa)]$^{2+}$ and [Pt(dmbpa)]$^{2+}$) that possessed high photostabilities and low cytotoxicities *via* chelation,[2b] and the products were developed as fluorogenic imaging probes specific for RNA G-quadruplexes in live cells (Fig. 1b). Zhu's team synthesized a carboplatin-based Pt(IV) prodrug functionalized with a boron dipyrromethene ligand at the axial position,[2c] which photoactivated the compound and improved the efficacies and selectivities (Fig. 1c). Apparently, the ligand structures were closely related to the photoreactivity, making a comprehensive understanding of the structure–optical performance relationship a key point in the fields of Pt-based detection and phototherapy. Taking advantage of density functional theory (DFT) studies and the development of time-dependent DFT (TD-DFT) methods, numerous theoretical

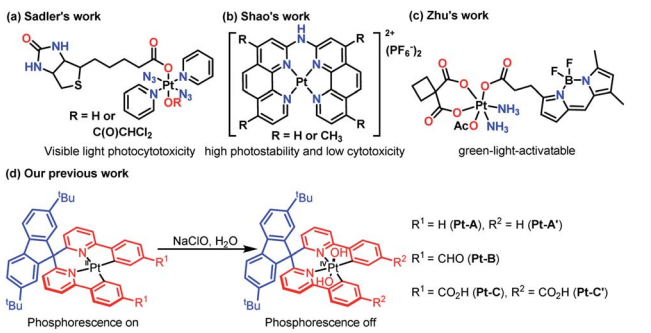

Fig. 1 Recent reported Pt(II)/Pt(IV) complexes.

[a]*Guangdong Provincial Key Laboratory of Chemical Measurement and Emergency Test Technology, Institute of Analysis, Guangdong Academy of Sciences (China National Analytical Center, Guangzhou), Guangzhou, 510070, P. R. China. E-mail: lzq@fenxi.com.cn*

[b]*School of Chemical Engineering and Technology, Sun Yat-sen University, Zhuhai, 519082, P. R. China*

[c]*School of Eco-Environmental Technology, Guangdong Industry Polytechnic, 152 Xingang West Road, Guangzhou, 510300, P. R. China. E-mail: 2015100029@gdip.edu.cn*

† Electronic supplementary information (ESI) available: Detailed results and coordinates of the optimized species. See https://doi.org/10.1039/d2ra03060h

works[3a,b] have focused on the excitation mechanisms for Pt-based compounds, which have promoted a better understanding of the optical performance and brought insights for advanced material design.

In our previous work, three Pt(II)–bisphenylpyridinylmethane complexes (**Pt-A**, **Pt-B**, and **Pt-C**) were synthesized and applied for the detection of hypochlorite ions through an oxidizing process,[4] during which Pt(IV) species (**Pt-A′** and **Pt-C′**) were yielded and turned phosphorescence off (Fig. 1d). Some preliminary DFT studies, including theoretical spectra interpretations and frontier orbitals visualizations, were incidentally performed. However, a few key points were not fully revealed, *e.g.* what was the role of the LK (Fig. 1d, coloured in blue) for absorption/emission, why did the oxidized Pt(IV) complexes lose phosphorescence, how were the electronic structures changed during the excitations process, *etc.* Answering these questions may supply a clearer understanding about the structure–optical performance relationship and pave the way for further structural renovations or performance modification works. In this paper, an in-depth theoretical study on the related Pt(II)/Pt(IV) complexes was performed focused on the geometric/electronic structures, and detailed mechanism in the absorption/emission process, as well as the relationship between the ligand structures and optical properties.

Computational details

For the purpose of investigating the SOC and accelerating computing, ORCA[5a–d] computational suite 5.0.0 was applied in this work. DFT methods, including B3LYP,[6a–c] PBE0 (ref. 6*d* and *e*), TPSS,[6f] and TPSSh[6f,g] were screened in geometry optimization tasks along with the Ahlrichs double-zeta basis set def2-SVP[6h,i] (standard) and def2-SVP/J[6i] (auxiliary), combining the D3 version of Grimme's dispersion[6j,k] in the gas phase. The resolution of identity (RI) approximation[6l,m] and tight SCF criteria were employed in the calculations. Frequency analysis was performed for the optimized structures at the same level and no virtual frequency was found, which ensured the optimization of the structures to a minimum point. The wavefunction generated at the PBE0-D3/def2-SVP level was selected for NCI studies[7a] and NBO analysis.[5e,7b–d] Excited states (ES) were calculated at the TD-PBE0/ZORA-def2-SVP[6n–s] level with the SARC-def2-SVP/J[6t] auxiliary basis set and RI-SOMF(1X)[6u] approximation. Also, the results were applied for hole–electron analysis,[7e] SOC studies, and absorption wavelength summaries. Triplet structures were optimized at the PBE0-D3/def2-SVP level by setting the multiplicity as 3, and the wavefunctions of the optimized structures were utilized to study the spin densities. Extractions of the energies and thermal correction values were realized by Shermo program.[5f] All the mentioned wavefunction analysis tasks were performed using the Multiwfn program.[5g] Root mean square displacement (RMSD) calculations and visualization of the structures and isosurface were completed using the VMD program.[5h] Also, mercury[5i] was applied for the bond distances measurements of the crystal and optimized structures.

Results and discussion

Geometric/electronic structure study

First, some well-resolved crystal structures[8a–c] of Pt complexes were optimized to screen the DFT methods with varied HF ratios, including TPSS (0%), TPSSh (10%), B3LYP (20%), and PBE0 (25%). The Pt–X (X = C, N, O, S) bond length deviations to those of crystal structures were chosen as standard, and PBE0 was found to be the optimal DFT method, which optimized the structures through the minimal RDSM and matched the bond lengths to the crystal structures to the greatest extent (more details in the ESI†).

As shown in Scheme 1, the mean Pt–X (X = C, N, O) bond lengths of the structures optimized by B3LYP, PBE0, and TPSSh are listed. Compared to the results optimized by PBE0, both B3LYP and TPSSh overestimated the Pt–X (X = C, N, O) bond distances by 1%. The average values of the Pt–N/Pt–C bonds were 2.089/1.996 Å in PBE0-optimized Pt(II) complexes, which were 0.5/0.3 Å longer than those in the reported paper. These elongated bond lengths indicated the lower stabilities of the related Pt(II) species, which provided the possibilities for further reactions. The Pt–N bond distance was extended to 2.117 Å after being oxidized, but the Pt–C bond length was almost unchanged, thereby implying the oxidization mainly affected the Pt–N bonds by weakening the coordination. It should be noted that the upside Pt–O bond (Pt–O87) was not identical to the downside one (Pt–O86) in the Pt(IV) species. Pt–O87 was about 0.1 Å shorter than the Pt–O86. One reason for this result may be attributed to the NCI formed by the *tert*-butyl benzene (^{t}BuPh) of the LK and hydroxyl groups (OH).

To confirm the inference, independent gradient modelling based on Hirshfeld partition (IGMH) analysis[7d] was performed and the isosurface was visualized using the BGR colouring method (more details in the ESI†). As shown in Fig. 2, the isosurface obviously pointed out the NCI between ^{t}BuPh and Pt/OH in **Pt-A**/**Pt-A′**. According to the colour filled on the isosurface, not only did van der Waals force (coloured in green) exist, but also H-bonds (coloured in blue) did too. Intensive repulsive interactions were not found because an orange/red isosurface did not appear. Namely, the attractive NCI was predominant in the space between ^{t}BuPh and Pt/OH. NCI was decomposed to

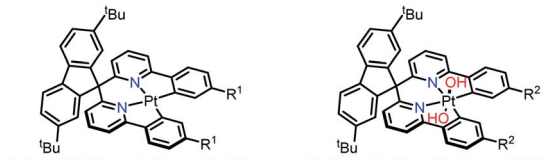

Pt-A	B3LYP	PBE0	TPSSh
Pt-N	2.114(5)	2.091(4)	2.096(5)
Pt-C	2.014(1)	1.998(0)	2.006(1)

Pt-B	B3LYP	PBE0	TPSSh
Pt-N	2.111(5)	2.088(5)	2.094(4)
Pt-C	2.012(1)	1.996(0)	2.005(1)

Pt-C	B3LYP	PBE0	TPSSh
Pt-N	2.111(5)	2.089(4)	2.090(0)
Pt-C	2.012(1)	1.995(1)	2.006(0)

Pt-A′	B3LYP	PBE0	TPSSh
Pt-N	2.139(1)	2.117(0)	2.123(2)
Pt-C	2.012(0)	1.995(0)	2.005(0)
Pt-O	2.033(11)	2.013(11)	2.029(9)

Pt-C′	B3LYP	PBE0	TPSSh
Pt-N	2.138(1)	2.117(1)	2.122(0)
Pt-C	2.011(0)	1.995(0)	2.005(1)
Pt-O	2.032(11)	2.014(11)	2.028(10)

Scheme 1 Pt–X (X = C, N, O) bond lengths (Å) optimized by different DFT methods.

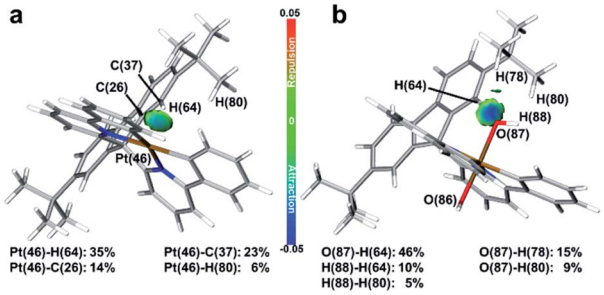

Fig. 2 IGMH isosurfaces of **Pt-A** and **Pt-A′**. (a) **Pt-A**; (b) **Pt-A′**; wavefunctions generated at PBE0-D3/def2-SVP were applied for IGMH analysis. BGR method ranged from −0.05 to 0.05 was applied for visualizing isosurface of IGMH.

atom pairs, and the contributions greater than 5% are listed on the bottom. We could clearly identify the great contribution of the aromatic hydrogen (H64) close to the central metal, which participated in the interaction with Pt/OH in **Pt-A**/**Pt-A′** and supplied over a one-third contribution. As we found in our former work,[9] the hindered structure may have affected the electronic structures and brought changes to the bond orders, as well as the atom charge populations.

NBO analysis was then performed to learn the details. The natural population analysis (NPA)[7c] charge of H64 in **Pt-A** was 0.2486, which was 0.0138 greater than the average values of other aromatic H atoms (ArH). Also, the natural electron configuration (NEC)[7b] of H64 was $1s^{0.75}$, which was 0.013 less. In brief, the NPA charges and NEC situations both indicated the charges transferring from H64, which should be a major contributor to NCI. As for **Pt-A′**, the NEC of the O87/O86 were similar, which were $2s^{1.80}2p^{5.16}3p^{0.01}$ and $2s^{1.80}2p^{5.13}3p^{0.01}$, respectively. However, the NPA charges of H64/average ArH were 0.2861/0.2374, and those of O87/O86 were −0.9670/−0.9451. Thus, the charge population deviations of the oxygen atoms could be assigned to the H-bond that transferred electrons from H64 to O87.

To summarize, the LK connected in the middle of the phenylpyridines were adjacent to Pt/OH in **Pt-A**/**Pt-A′**. The closeness of these atoms brought van der Waals attractions and H-bonds in to play, which further affected the electronic structures, enriching the charge population of the O87 and shortening the Pt–O87 bond.

Excited states analysis

With the optimized structures in hand, we then carried out further studies on the excitation mechanisms. As we confirmed in our previous work, the ground states (GS) of the related Pt(II)/Pt(IV) complexes were singlets (S_0). Hole–electron analysis was performed as a start to grasp the detailed information of what occurs during the excitation process.

As shown on the left of each thumbnail, the oscillatory strengths (OS) of the Pt(II)/Pt(IV) excited singlet states (S_n) were visualized by heatmaps using grayscale, with values ranging from 0 (white) to 0.4 (black). The maximal OS of the Pt(II) species were greater than those of Pt(IV) (0.2826, 0.3924, 0.2918 *vs.* 0.1904, 0.2112).

The OS values were related to the transaction efficiencies, that is, it was easier to form ES for Pt(II) species. The maximal OS of S_n ($n < 10$) in Pt(II) were 4–5 times the Pt(IV) ones, indicating the low-level ES were much harder to form after oxidation. In other words, the oxidized Pt(IV) species tended to be excited to higher energy levels with inferior efficiencies, which led to lower abundances of ES and more losses when high-energy-level ES went back to S_n ($n \leq 5$).

The hole and electron isosurfaces were then visualized, and the blue/white isosurfaces represent electrons/holes where the electrons flowed in/out and the density of electrons increased/decreased during the excitation process. Besides, the complex structures were divided into fragments to study how the structures played a role in the optical performance. Pt(II) species were divided into three parts, the LK, Pt, and bisphenylpyridines (LG), while the Pt(IV) species had one more part, the OH. As shown on the bottom of each thumbnail, the heatmaps expressed the contributions of the fragments to holes (H), electrons (E) and overlaps (O) using white to black gradient ranging from 0 to 100%. Combined with the results shown in Fig. 3, the following details were obtained:

(a) The low-level ES ($S_0 \rightarrow S_n$, $n \leq 6$) in Pt(II) species formed by metal-to-ligand charge-transfer excitation (MLCT). In this procedure, LG comprised the vast majority of electrons. Electrons transfer from the central metal and part of the LG to the remaining part of LG, while LK hardly participates in the charge transfer; (b) high-level ES ($S_0 \rightarrow S_n$, $n > 15$) with the maximal OS in Pt(II) species were generated by a local excitation (LE) mechanism, which mainly occurred on the LP, and LK contributed a small part. Since the holes and electrons are both mainly distributed on LP, making the transition dipole moments effectively overlap, the OS had the maximum values in these situations; (c) the low-level ES in Pt(IV) were promoted by the charge-transfer (CT) mechanism, among which the holes and electrons were distinctly separated. However, the detailed procedure in **Pt-C′** ($S_0 \rightarrow S_6$) differed from that of **Pt-A′** ($S_0 \rightarrow S_2$). Specifically, LK contributed holes in a very high proportion at **Pt-C′** while Pt or OH were nearly invalid. The situation was reversed in **Pt-A′**. The far separation of holes and electrons decreased the transition dipole moments, which resulted in the OS weakening of **Pt-A′** and **Pt-C′** in the low-level ES; (d) the high-level ES in Pt(IV) were yielded by an LE process, in which the involved parts in **Pt-A′** were Pt, LG, and OH, while those in **Pt-C′** were LK, LG, and OH. In this case, LG also played a role as the acceptor for electrons flowing in, and the remaining part mainly played the role of a donor for electrons flowing out.

To conclude, LG was the main part for accepting electrons in these Pt complexes during the excitation process, and therefore its structure should be a core factor affecting the OS. The electron-withdrawing groups (EWG) embedded on LG took advantages in enhancing the attraction to electrons and stabilizing the ES after electrons migrated in. That is the reason why **Pt-B** and **Pt-C** had a greater maximal OS than **Pt-A**. The LK mostly played the role of electron donors in the excitation process, while the non-coplanarity and far distances to LG made

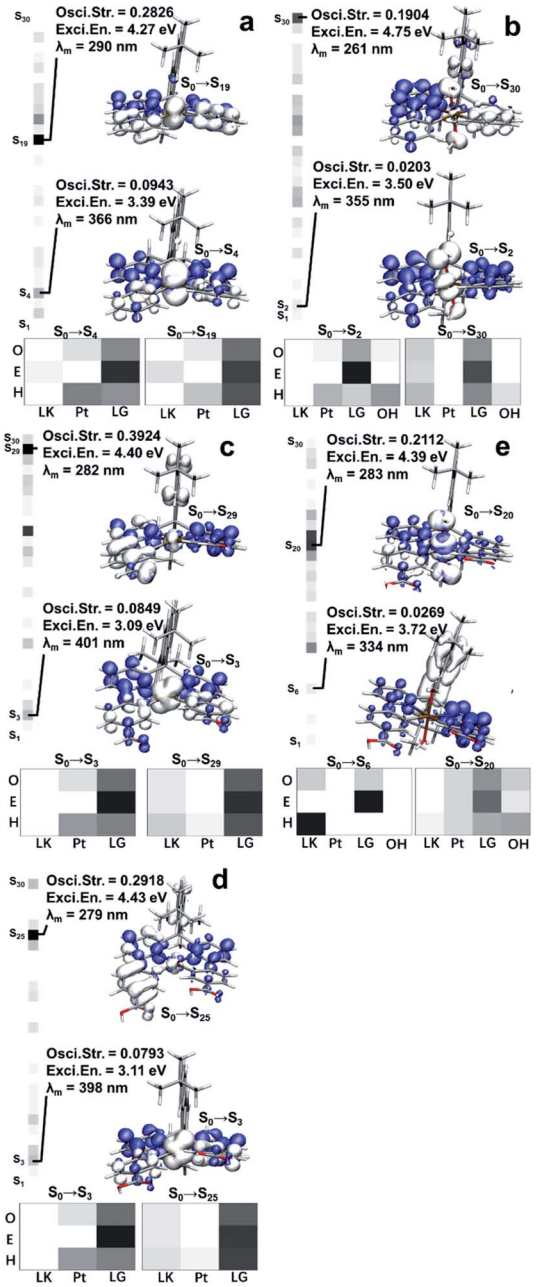

Fig. 3 Hole–electron studies and visualizations of the Pt(II)/Pt(IV) complexes. (a) **Pt-A**; (b) **Pt-B**; (c) **Pt-C**; (d) **Pt-A′**; (e) **Pt-C′**. Wavefunctions and output files generated at TD-PBE0-D3/ZORA-def2-SVP were applied for hole–electron analysis. The oscillatory strengths were visualized on the left of each thumbnail by heat map using grayscale ranged from 0 to 0.4. Hole–electron isosurface were visualized by VMD and the blue isosurface represented for electron while the white ones represented for hole. Contributions of the fragments were visualized by heat map using white to black gradient ranged from 0 to 100%.

the LE mechanism have poor efficiency. Accordingly, we believe the modification of the LK with EWG may impair the LE process by cutting down electrons flowing out from the LK. Alternatively, the efficient LE occurring on the LG part may increase, through which the excitation efficiencies could be improved for these Pt species. As for OH, they were the holes in the excitation process, but the overlapping of the hole isosurface in OH and the electron isosurface in LG was inefficient. Hence, the higher electron density OH possessed, the lower the excitation efficiency would be. Combining the results from NBO analysis, H64 in LK donated electrons to O87 by forming H-bonds, which enriched the electron abundances of OH and deteriorated the excitation efficiency. Further, OH belonged to a kind of EWG, which attract the electrons in Pt and hinder its transferring, resulting in the MLCT mechanism became useless in Pt(IV). Putting these results together shows the whole reason for the OS weakening and absorption efficiencies declining in Pt(IV) complexes.

According to the experimental spectra, the emission process obeyed Kasha's rule,[10] whereby the ES went back to the GS through the first excited triplet states (T_1). Consequently, an intersystem crossing (ISC) process was involved for S_n transforming into triplet ES (T_n). SOC reflects the interactions between the electron spin and electron orbital motion, which the alleviated ISC ban and was a key point to reveal the on–off phosphorescence phenomenon. The details of T_1 going back to the GS considering the SOC are shown in Fig. 4. We can see T_1 could be split into three sublevels with closed energies after considering the SOC, and their OS values are noted in the corresponded colours. The energy levels of the Pt(II) species were about 3000 cm^{-1} lower than the Pt(IV) ones, and the corresponding OS varied from 0.00002 to 0.00103. The lifetime of the T_1 sublevels were then calculated by Einstein's equation.[11] The maximal lifetime values of the sublevels are listed on the bottom of each compound, and we can see which had minor differences (**Pt-A**: 2.1; **Pt-B**: 6.0; **Pt-C**: 0.83; **Pt-A′**: 0.32; **Pt-C′**: 1.9, unit 10^{-4} s). In other words, the related Pt complexes possessed similar T_1 lifetimes, and therefore the process of T_1 returning to S_0 was not the reason for the phosphorescence quenching of Pt(IV) species.

To further investigate the phosphorescence quenching mechanism, S_n ($n \leq 20$) and T_n ($n \leq 20$) were taken into consideration. Also, SOCME results whose values characterized the degree of ISC were selected for careful discussion. As shown in Fig. 5, the processed SOCMEs[12] were visualized by heatmaps (more details in ESI).

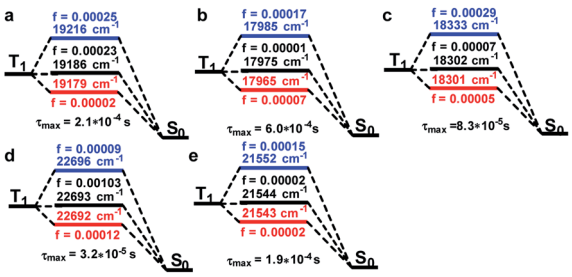

Fig. 4 Details of the phosphorescence emission from T_1 to S_0. (a) **Pt-A**; (b) **Pt-B**; (c) **Pt-C**; (d) **Pt-A′**; (e) **Pt-C′**. SOC was calculated at TD-PBE0-D3/ZORA-def2-SVP level. And the lifetimes were calculated by Einstein's fromula: $\tau = 1.5/(f \times E^2)$, and the maximal τ of the splitted sublevel was listed.

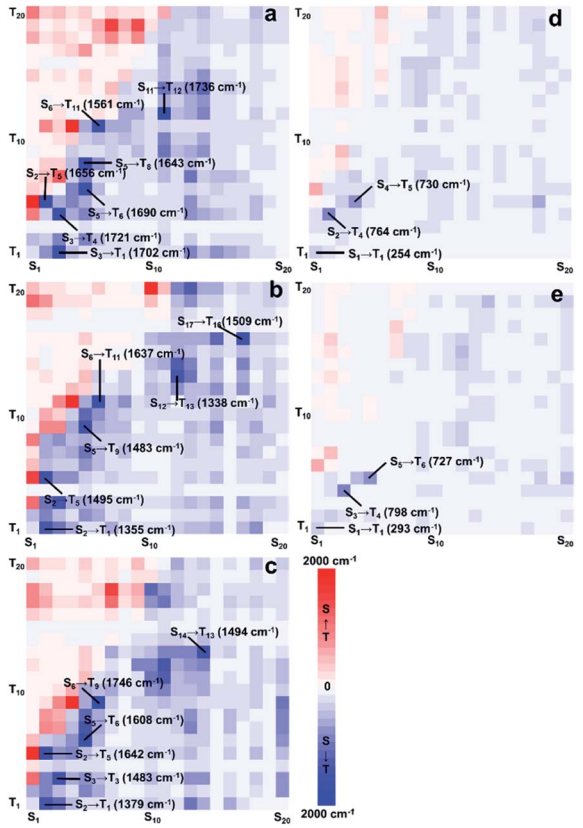

Fig. 5 SOCME heatmap of the Pt(II)/Pt(IV) complexes. (a) **Pt-A**; (b) **Pt-B**; (c) **Pt-C**; (d) **Pt-A′**; (e) **Pt-C′**. SOC was calculated at TD-PBE0-D3/ZORA-def2-SVP level, and 20 states were considered. The SOC matrix elements were proceeded by Chou's method and visualized by heat map using BWR coloring method ranged from 0 to 2000 cm^{-1}, by which red represented for SOC of singlets to triplets (S → T) while blue represented the opposite (T → S).

The BWR colouring method was applied to visually exhibit the values of SOCME, in which the blue grid points represent the SOC of ISC, while the red ones represent those for the reverse ISC (RISC). The shade of the colours is proportional to the SOCME and some extremums are listed. It can be distinctly seen that ISC and RISC were both remarkably weakened in Pt(IV) complexes, because the colour filled in Fig. 5d and e turned pale. The extremums to form T_1 were 1702, 1355, and 1379 cm^{-1} for **Pt-A**, **Pt-B**, and **Pt-C**, respectively, which were about 5–7 times greater than those in Pt(IV) species (254 and 293 cm^{-1}). Combining the conclusion drawn out by the ES analysis that Pt(II) species possessed greater OS to form low-level ES, T_1 could be generated through the $S_m \rightarrow T_n \rightarrow T_1$ or $S_m \rightarrow S_n \rightarrow T_1$ ($m < 5$, $n < m$) pathways in higher yields. The high-level ES of Pt(II) species were also easier to be generated, and the highly efficient ISC/RISC extended the lifetime of the ES for the Pt(II) species, which provided long-lived ES and increased the phosphorescent emission intensities. On the contrary, the ES of the Pt(IV) species preferred to be yielded in high levels, and the weak ISC strengthened the non-radiative transitions, which made the $S_m \rightarrow T_n \rightarrow T_1$ or $S_m \rightarrow S_n \rightarrow T_1$ ($m > 7$, $n < m$) pathways inefficient. In short, the greatly reduced abundances of T_1 in Pt(IV) species was a main reason for the phosphorescence quenching.

The excitation types of T_1 and those of the related S_n were then visualized to dig out the more fundamental principles. As shown in Fig. 6, hole–electron isosurfaces of the ES with the maximal SOCME corresponded to $S_n \rightarrow T_1$ are visualized. The excitation types of all the related S_n were MLCT, including Pt(II) and Pt(IV) species, and those of T_1 in the Pt(II) species were MLCT too. However, the excitation types of T_1 in the Pt(IV) species were mainly contributed to by LE, in which the central metal contributed little. In short, the T_1 and S_n had the same nature for Pt(II) complexes, while those in Pt(IV) ones were different. So, the ISC process of these complexes did not obey El-Sayed's rule that triplet and singlet conversions in cases where the states have the same nature are prohibited.[13a,b] It was speculated that the relativistic effects caused by Pt was more significant, and SOC interacted more efficiently when the electrons were constrained on the heavy metal, which overcame the disapproval of El-Sayed's rule.

Next, the T_1 structures were optimized to investigate the spin situation and NBO analysis was utilized to elucidate the electronic structure details. Taking **Pt-A** and **Pt-A′** as examples, their natural spin densities (NSD) are listed in Fig. 7 alongside the spin density isosurface. By referring to the NSD values, we found a single electron partially distributed on the central metal (0.24), the C atom (0.35) and N atom (0.24) connected to Pt for **Pt-A**. Differently, it did not distribute on Pt for triplet **Pt-A′**, and was mostly located on the relatively remote *para*-site of Pt (0.47, 0.45).

The contributions of each orbital to generate single electrons was further decomposed, and the 5d orbitals that participated were $5d_{xy}$, $5d_{xz}$, and $5d_{x^2-y^2}$ in **Pt-A**, which supplied 0.06, 0.09, and 0.06 single electrons, respectively. However, the corresponding orbitals contributed much less in **Pt-A′**, whose values were 0.01($5d_{xy}$), 0.01($5d_{xz}$), and 0.02($5d_{x^2-y^2}$). Also, the hybrid type of Pt in Pt(II)/Pt(IV) species was $dsp^2/d2sp^3$, in which 4/3 pairs of lone pair electrons (LP) were settled in d orbitals.

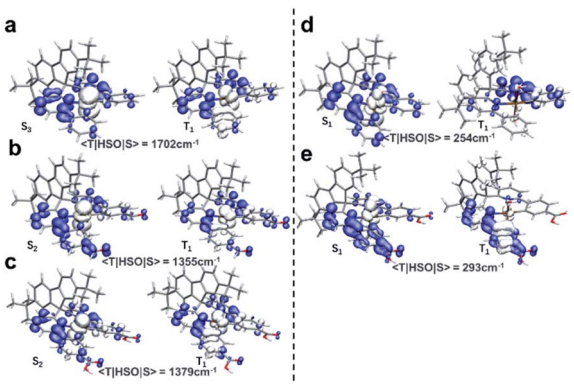

Fig. 6 Excitation types of T_1 and related S_n of the Pt(II)/Pt(IV) complexes. (a) **Pt-A**; (b) **Pt-B**; (c) **Pt-C**; (d) **Pt-A′**; (e) **Pt-C′**. Wavefunctions and output files generated at TD-PBE0-D3/ZORA-def2-SVP were applied for hole–electron analysis. Hole–electron isosurface were visualized by VMD and the blue isosurface represented for electron while the white ones represented for hole.

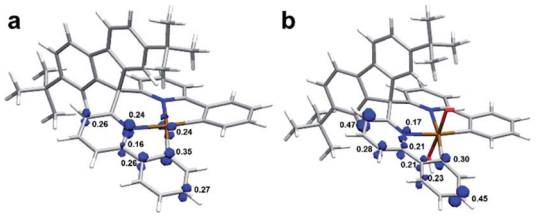

Fig. 7 Spin density of triplet **Pt-A** and **Pt-A′**. (a) **Pt-A**; (b) **Pt-A′**; wavefunctions generated at PBE0-D3/def2-SVP (triplet) were applied for spin density analysis, isovalue 0.025.

Basically, spin–flip could be realized by LP excitation. The LP in **Pt-A** were less restrained without the strong bonding of OH, which made it easier to accomplish spin–flip through electron excitation, while the similar mechanism did not work for **Pt-A′**. Without the contribution of a central atom, spin–flip was much harder to achieve only by SOC, which responded to the low efficiency of $S_n \rightarrow T_1$, and resulted in the phosphorescence-off phenomenon for Pt(IV) complexes.

Conclusion

In summary, we confirmed the reasonability of the DFT method PBE0 in optimization tasks for the reported Pt complexes. Through NBO analysis and NCI discussion, we found the LK promoted the upside Pt–O bond strengths by forming H-bonds and providing van der Waals attractions, which revealed the reasons for the inequalities between Pt–O bonds in Pt(IV) complexes. Electron–hole analysis indicated that LG with an EWG embedded, such as carboxyl, aldehyde, nitro, possessed superior excitation efficiencies, while LK with the same had the opposite effect, leading to a poor yield of excitation states. Hence, a rational ligand design to improve the excitation efficiencies was to decorate the LK with an EDG, such as alkyl, alkoxy, alkylamino, and to modify the LG with an EWG. The mechanism of phosphorescence quenching in Pt(IV) species was carefully explored through hole–electron analysis and the newly-developed visualization method for SOCME. The oxidation-caused phosphorescence-off was most likely due to the deteriorated excitation efficiencies and weakened ISC to form T_1 species rather than El-Sayed's rule or lifetimes differences. The strong impact of a central metal significantly improved the ease of spin–flip in Pt(II) complexes, which was impaired by the electron-withdrawing effect of the OH connected in the Pt(IV) species. In other words, replacing OH with another EWG in Pt(IV) species should also exhibit identical on–off phosphorescence performance, which could be applied in the wider field of detection research. This in-depth result should be broadly applicable to the cases of similar compounds. Furthermore, we disclosed how the substituents on the LK and LG affected the excitation efficiencies, which will bring insight to the structural design in further research.

Conflicts of interest

There are no conflicts to declare.

Acknowledgements

This work was supported by the funding of Education Commission of Guangdong Province (2020ZDZX2077), Special Fund Projects of Guangdong Academy of Sciences for the Construction of Domestic First-class Research Institutions (2021GDASYL-20210103035), and Science and Technology Planning Project of Guangzhou (202102021119).

Notes and references

1 Reviews or papers on the applications of Pt complexes, see:(*a*) H. Chen, Y. Li, S. Liu, Q. Xiong, R. Bai, D. Wei and Y. Lan, *Coord. Chem. Rev.*, 2021, **437**, 213863; (*b*) C. Jia, G. B. Deacon, Y. Zhang and C. Gao, *Coord. Chem. Rev.*, 2021, **429**, 213640; (*c*) M. Mbaba, T. M. Golding and G. S. Smith, *Molecules*, 2020, **25**, 5276–5307; (*d*) C. F. Chow, F. W. Gong and C. B. Gong, *Analyst*, 2014, **139**, 4532–4537; (*e*) C.-S. Chu, T.-W. Sung and Y.-L. Lo, *Sens. Actuators, B*, 2013, **185**, 287–292; (*f*) J. B. Reyes, M. K. Kuimova and R. Vilar, *Curr. Opin. Chem. Biol.*, 2021, **61**, 179–190; (*g*) C. Cebrian and M. Mauro, *Beilstein J. Org. Chem.*, 2018, **14**, 1459–1481.

2 For selected papers on the newly synthesized Pt complexes, see:(*a*) H. Shi, C. Imberti, H. Huang, I. Hands-Portman and P. J. Sadler, *Chem. Commun.*, 2020, **56**, 2320–2323; (*b*) L. He, Z. Meng, Q. Guo, X. Wu, M. P. Teulade-Fichou, E. K. L. Yeow and F. Shao, *Chem. Commun.*, 2020, **56**, 14459–14462; (*c*) H. Yao, S. Chen, Z. Deng, M. K. Tse, Y. Matsuda and G. Zhu, *Inorg. Chem.*, 2020, **59**, 11823–11833.

3 For selected papers on the DFT study about Pt complexes, see: (*a*) S. P. Wang, Y. Li, Z. X. Zhang, Y. Zhang, Y. Wang, S. M. Kong, H. C. Li, W. Jian, F. Q. Bai and H. X. Zhang, *Inorg. Chem.*, 2021, **60**, 1480–1490; (*b*) T. Eskelinen, S. Buss, S. K. Petrovskii, E. V. Grachova, M. Krause, L. Kletsch, A. Klein, C. A. Strassert, I. O. Koshevoy and P. Hirva, *Inorg. Chem.*, 2021, **60**, 8777–8789.

4 J. Tang, G. Zhu, P. Li, P. Zhang, F. Peng and F. Meng, *Analyst*, 2021, **146**, 5691–5703.

5 Software and program involved in this paper, see:(*a*) F. Neese, *Wiley Interdiscip. Rev.: Comput. Mol. Sci.*, 2012, **2**, 73–78; (*b*) F. Neese, *Wiley Interdiscip. Rev.: Comput. Mol. Sci.*, 2018, **8**, e1372; (*c*) F. Neese, F. Wennmohs, U. Becker and C. Riplinger, *J. Chem. Phys.*, 2020, **152**, 224108; (*d*) F. Neese, *Wiley Interdiscip. Rev.: Comput. Mol. Sci.*, 2022, 1–15; (*e*) E. D. Glendening, C. R. Landis and F. Weinhold, *J. Comput. Chem.*, 2019, **40**, 2234–2241; (*f*) T. Lu and Q. Chen, *Comput. Theor. Chem.*, 2021, **1200**, 113249; (*g*) T. Lu and F. Chen, *J. Comput. Chem.*, 2012, **33**, 580–592; (*h*) H. William, D. Andrew and S. Klaus, *J. Mol. Graphics*, 1996, **14**, 33–38; (*i*) C. F. Macrae, I. Sovago, S. J. Cottrell, P. T. A. Galek, P. McCabe, E. Pidcock, M. Platings, G. P. Shields, J. S. Stevens, M. Towler and P. A. Wood, *J. Appl. Crystallogr.*, 2020, **53**, 226–235.

6 Methods involved in DFT calculations, see:(*a*) A. D. Becke, *J. Chem. Phys.*, 1993, **98**, 5648–5652; (*b*) C. Lee, W. Yang and R. G. Parr, *Phys. Rev. B: Condens. Matter Mater. Phys.*, 1988,

37, 785–789; (*c*) B. Miehlich, A. Savin, H. Stoll and H. Preuss, *Chem. Phys. Lett.*, 1989, **157**, 200–206; (*d*) J. P. Perdew, K. Burke and M. Ernzerhof, *Phys. Rev. Lett.*, 1996, **77**, 3865–3868; (*e*) J. P. Perdew, K. Burke and M. Ernzerhof, *Phys. Rev. Lett.*, 1996, **78**, 1396; (*f*) J. Tao, J. P. Perdew, V. N. Staroverov and G. E. Scuseria, *Phys. Rev. Lett.*, 2003, **91**, 146401; (*g*) V. N. Staroverov, G. E. Scuseria, J. Tao and J. P. Perdew, *J. Chem. Phys.*, 2003, **119**, 12129–12137; (*h*) F. Weigend and R. Ahlrichs, *Phys. Chem. Chem. Phys.*, 2005, **7**, 3297–3305; (*i*) F. Weigend, *Phys. Chem. Chem. Phys.*, 2006, **8**, 1057–1065; (*j*) S. Grimme, J. Antony, S. Ehrlich and H. Krieg, *J. Chem. Phys.*, 2010, **132**, 154104; (*k*) S. Grimme, S. Ehrlich and L. Goerigk, *J. Comput. Chem.*, 2011, **32**, 1456–1465; (*l*) A. K. Dutta and F. Neese, *J. Chem. Phys.*, 2016, **144**, 034102; (*m*) G. J. Christan, F. Neese and S. F. Ye, *Inorg. Chem.*, 2016, **55**, 3853–3864; (*n*) E. van Lenthe, J. G. Snijders and E. J. Baerends, *J. Chem. Phys.*, 1996, **105**, 6505; (*o*) C. V. Caillie and R. D. Amos, *Chem. Phys. Lett.*, 1999, **308**, 249–255; (*p*) C. V. Caillie and R. D. Amos, *Chem. Phys. Lett.*, 2000, **317**, 159–164; (*q*) S. Hirata and M. Head-Gordon, *Chem. Phys. Lett.*, 1999, **314**, 291–299; (*r*) J. Liu and W. Liang, *J. Chem. Phys.*, 2011, **135**, 014113; (*s*) M. E. Casida, C. Jamorski, K. C. Casida and D. R. Salahub, *J. Chem. Phys.*, 1998, **108**, 4439–4449; (*t*) D. A. Pantazis, X. Y. Chen, C. R. Landis and F. Neese, *J. Chem. Theory Comput.*, 2008, **4**, 908; (*u*) F. Neese, *J. Chem. Phys.*, 2005, **122**, 034107.

7 Methods involved in wavefunction analysis, see:(*a*) E. R. Johnson, S. Keinan, P. Mori-Sánchez, J. Contreras-Garcí, A. J. Cohen and W. Yang, *J. Am. Chem. Soc.*, 2010, **132**, 6498–6506; (*b*) E. R. Alan and W. Frank, *J. Chem. Phys.*, 1983, **78**, 4066–4073; (*c*) A. E. Reed, R. B. Weinstock and F. Weinhold, *J. Chem. Phys.*, 1985, **83**, 735–746; (*d*) J. E. Carpenter and F. Weinhold, *J. Mol. Struct.: THEOCHEM*, 1988, **169**, 41–62; (*e*) Z. Liu, T. Lu and Q. Chen, *Carbon*, 2020, **165**, 461–467; (*f*) T. Lu and Q. Chen, *J. Comput. Chem.*, 2022, **43**, 539–555.

8 Single crystals applied for DFT method screening were obtained from CCDC database, see:(*a*) L. Niu, G. Ren, T. Hou, X. Shen and D. Zhu, *Inorg. Chem. Commun.*, 2021, **130**, 108737; (*b*) V. Cîrcu, M. Ilie, M. Iliș, F. Dumitrașcu, I. Neagoe and S. Păsculescu, *Polyhedron*, 2009, **28**, 3739–3746; (*c*) M. Tan, Z. Wang, Q. Qin, X. Huang, B. Zou and H. Liang, *Inorg. Chem. Commun.*, 2019, **108**, 107510.

9 G. Zhu, A. You, H. Song and Z. Li, *RSC Adv.*, 2022, **12**, 10014–10019.

10 N. Lewis and M. Kasha, *J. Am. Chem. Soc.*, 1944, **66**(12), 2100–2116.

11 R. C. Hilborn, *Am. J. Physiol.*, 1982, **50**, 982–986.

12 E. Y. Li, T. Jiang, Y. Chi and P. Chou, *Phys. Chem. Chem. Phys.*, 2014, **16**, 26184–26192.

13 (*a*) S. K. Lower and M. A. El-Sayed, *Chem. Rev.*, 1966, **66**, 199–241; (*b*) M. A. El-Sayed, *Acc. Chem. Res.*, 1968, **1**, 8–16.